

Characterizing point spread functions of two-photon fluorescence microscopy in turbid medium

Chen-Yuan Dong

National Taiwan University
Microscopic Biophysics Laboratory
Department of Physics
Taipei 106
Taiwan

Karsten Koenig

Friedrich Schiller University Jena
Institute of Anatomy II
Teichgraben 7
D-07743 Jena
Germany

Peter So

Massachusetts Institute of Technology
Department of Mechanical Engineering
77 Massachusetts Ave.
Cambridge, Massachusetts 02139
USA
E-mail: pts@mit.edu

Abstract. In recent years, fluorescence microscopy based on two-photon excitation has become a popular tool for biological and biomedical imaging. Among its advantages is the enhanced depth penetration permitted by fluorescence excitation with the near-infrared photons, which is particularly attractive for deep-tissue imaging. To fully utilize two-photon fluorescence microscopy as a three-dimensional research technique in biology and medicine, it is important to characterize the two-photon imaging parameters in a turbid medium. We investigated the two-photon point spread functions (PSFs) in a number of scattering samples. Gel samples containing 0.1- μm fluorescent microspheres and Liposyn III were used as phantoms mimicking the turbid environment often found in tissue. A full characterization of the two-photon PSFs of a water and oil immersion objective was completed in samples composed of 0, 0.25, 0.5, 1, and 2% Liposyn III. Our results show that up to depths of about 100 (oil) and 200 μm (water), the presence of scatterers (up to 2% Liposyn III) does not appreciably degrade the PSF widths of the objectives. © 2003 Society of Photo-Optical Instrumentation Engineers. [DOI: 10.1117/1.1578644]

Keywords: fluorescence; microscopy; near infrared; medicine.

Paper JBO 02061 received Sep. 3, 2002; revised manuscript received Mar. 14, 2003; accepted for publication Mar. 17, 2003.

1 Introduction

Since the experimental realization of two-photon imaging by Webb's group in 1990,¹ this technique has found broad applications in biology and medicine. Compared with conventional, single-photon excitation microscopic techniques, a number of significant advantages popularized two-photon microscopy. To begin with, the nonlinear nature of two-photon excitation limits fluorescence generation to the focal volume. When an objective with a high numerical aperture is used, the dimension of the focal spot is about 0.3 μm (radial) and 0.7 μm (axial), corresponding to a localized volume on the order of 0.1 fL.² Microscopic imaging by raster scanning a pointlike, two-photon spot results in an axial sectioning effect similar to that found in confocal microscopy. The few fluorescent photons generated in the off-focal region interfere little with focal imaging. As a result, image quality is greatly improved and photodamage is limited. Discussions of confocal and two-photon microscopy can be found in the literature (for example, see Ref. 3). Furthermore, the near-infrared (IR) photons used for two-photon excitation of visible fluorescent probes are scattered and absorbed less by biological specimens than the UV/visible photons used in one-photon absorption.^{3,4,5} Therefore, greater depth penetration can be achieved by two-photon microscopy. Finally, since the near-IR wavelength used for sample excitation is spectrally well separated from typical fluorescence emissions, the complete fluorescence emission spectrum can be more easily obtained by two-photon excitation. These unique characteristics make two-photon excitation a very attractive experimental technique for biomedical imaging, especially in optically opaque samples. For example, human and mouse skin has

been extensively imaged by two-photon microscopy.^{6,7} Corneal structure has also been examined.^{8,9} Two-photon microscopy has also found significant applications in neurobiology and embryology. Neurons and dendrites have been extensively investigated^{10–13} and processes such as sperm–egg fusion and embryo development have also been studied.^{14,15} In fact, a comparative study between confocal and two-photon microscopy shows that in a number of biological specimens, two-photon microscopy can penetrate at least twice as deep as confocal microscopy.¹⁶ With further development, two-photon fluorescence microscopy can become a powerful technique for *in vivo* diagnosis of epithelial diseases.

2 In-depth Characterization of the Two-Photon Point Spread Function

Optical imaging of optically thick biological specimens can be hampered by photon interaction with tissue constituents. For example, tissue absorption and scattering can limit the useful range of depth penetration. Both the absorption and scattering coefficients of many tissue types have been characterized. It was found that in the red/near-IR range, the absorption, scattering, and reduced scattering coefficients are around 0.01 to 1 mm^{-1} , 1 to 100 mm^{-1} , and 0.1 to 5 mm^{-1} , respectively.^{17–19} In the literature, a number of groups have reported investigation of the imaging characteristics of two-photon microscopy in a turbid medium.^{16,20–25} In particular, some groups reported negligible effects on the point spread function (PSF), owing to scattering.^{16,25} However, there has also been at least one report in which it was demonstrated that

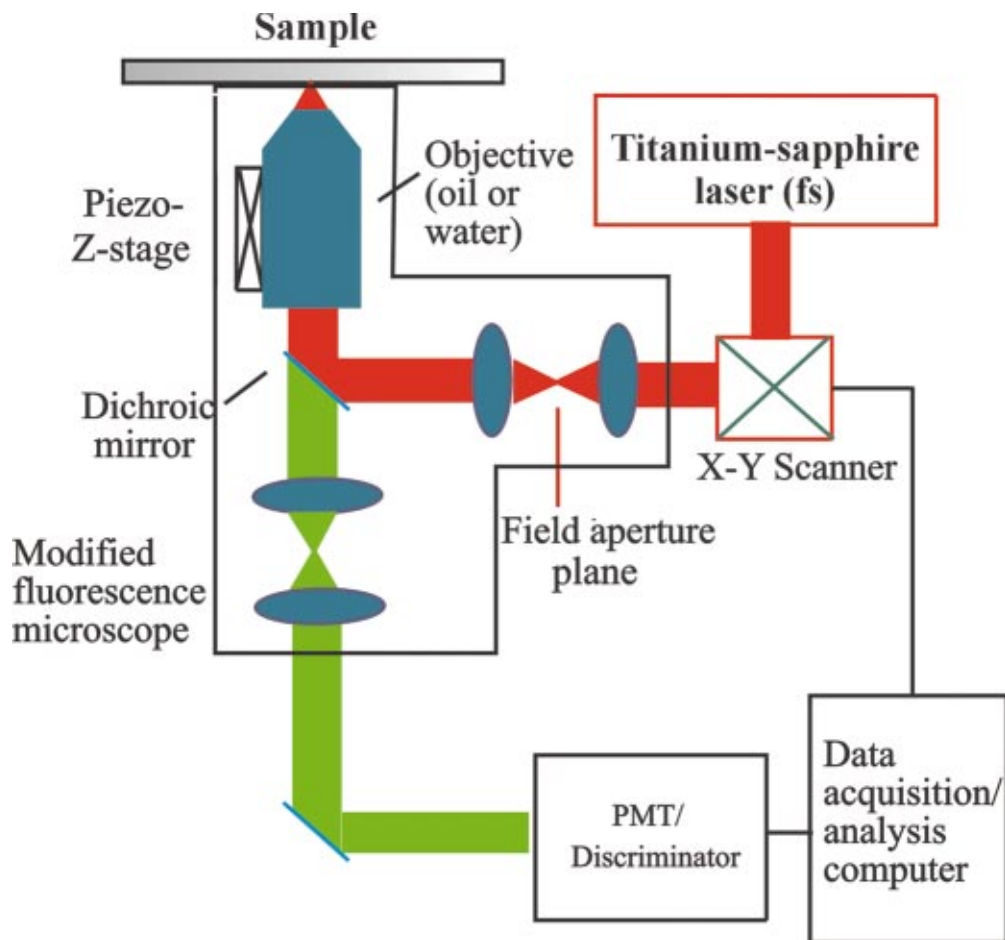
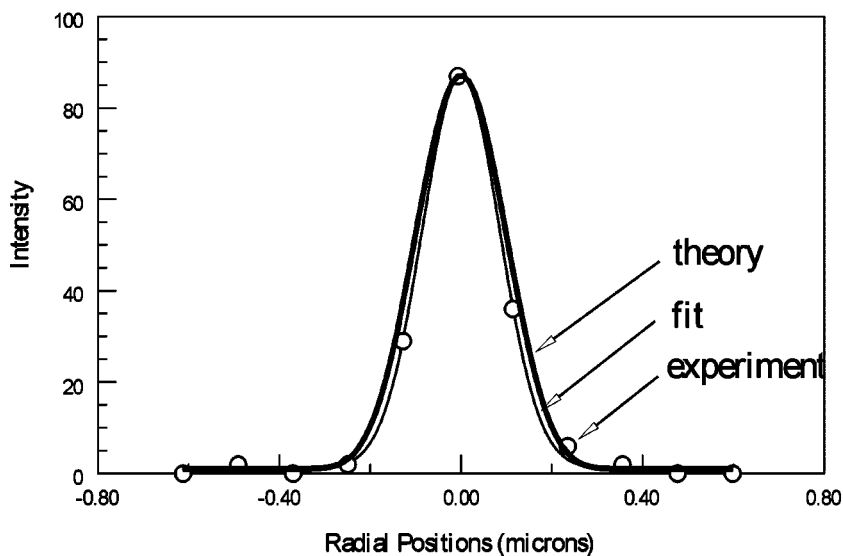


Fig. 1 A two-photon fluorescence microscope using a femtosecond Ti:S laser.



Fig. 2 A representative three-dimensional scan of multiple microspheres ($0.1 \mu\text{m}$). Image taken near the surface using the $63\times$ oil objective volume data of the microspheres.

Radial Intensity for 63x Plan-Neofluar Objective (Surface)



Axial Intensity for 63x Plan-Neofluar Objective (Surface)

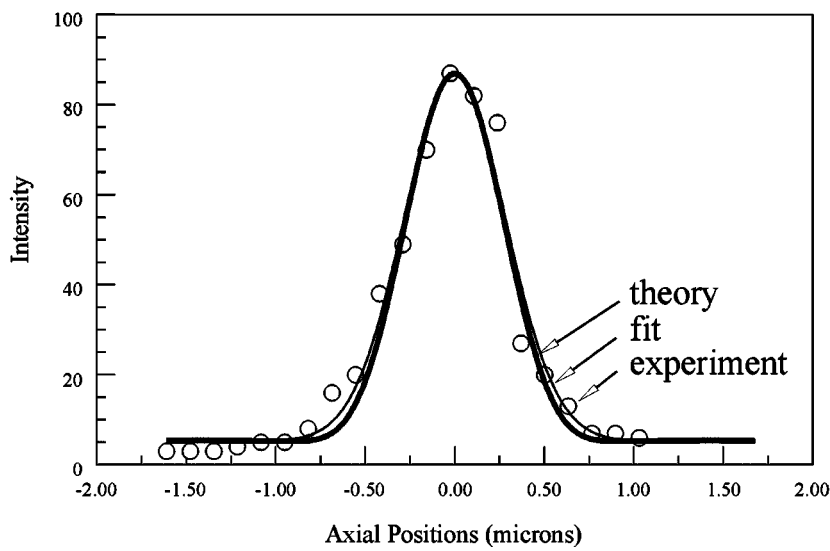


Fig. 3 The radial and axial PSF plots for the sphere chosen in Fig. 2. Experimental data, results of the Gaussian fit, and theoretical distributions are shown.

the two-photon image resolution degrades in the presence of scattering microspheres.²⁶ Nonetheless, to the best of our knowledge, a complete characterization of the PSF in media with different scattering properties with both oil and water immersion objectives is absent in the literature.

In this paper we address this issue by characterizing the two-photon PSF in a number of turbid media. Agarose gel samples imbedded with 0.1-μm fluorescent beads in different lipid emulsions were made and imaged. For a thorough study, lipid emulsion concentrations at 0, 0.25, 0.5, 1, and 2% were made. At these concentrations, the reduced scattering coefficients around 620 nm are approximately 0, 0.38, 0.75, 1.5, and 3 mm⁻¹ for the respective concentrations.²⁷ A recent

study has shown that μ_s and $\mu_{s'}$ for comparable 2% Intralipid to be 6 and 2.1 mm⁻¹, respectively (at 780 nm).²⁵ These values demonstrate that the scattering properties of the samples we prepared match well with those of many tissue types and that they are fair representations of tissuelike phantoms.¹⁸

3 Experimental Apparatus

The two-photon fluorescence microscope used in this study is shown in Fig. 1. An argon ion (Innova 300, Coherent Inc., Santa Clara, California)-pumped, femtosecond titanium:sapphire (Ti:S) laser (Mira 900, Coherent Inc.) is the source of

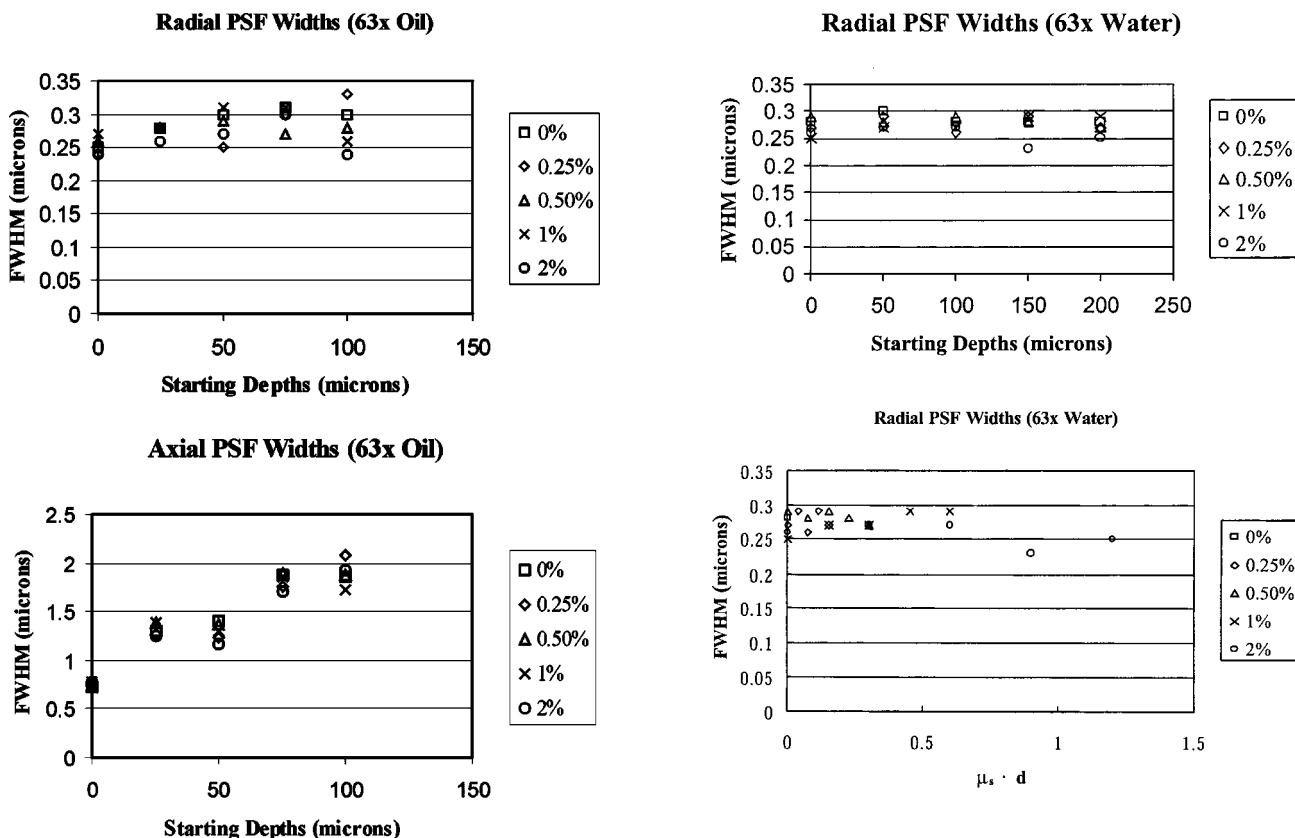


Fig. 4 Averaged widths of the radial and axial PSFs from five spheres at two depths and five Liposyn III concentrations (0, 0.25, 0.5, 1, and 2%), taken with 63 \times , oil immersion, Plan-Neofluar objective (NA 1.25).

two-photon excitation. The broad lasing range (approximately 700 to 1000 nm) of the Ti:S laser can be used for the excitation of a wide range of visible fluorescent molecules. For the imaging of our 0.1- μm spheres, a 780-nm wavelength was used. Before entering the modified fluorescent microscope used in this study (Axiovert 100TV, Carl Zeiss Inc., Thornwood, New York), the laser beam passes through an x-y scanner (model 6350, Cambridge Technology, Cambridge, Massachusetts). The scanning mirror-driven, angular deviations of the laser beam are translated into linear positions of the focal spot at the sample. To ensure overfilling of the objective's back aperture, a beam expander is positioned between the x-y scanner and the objective.

The expanded laser beam is reflected into the back aperture of the objective by a short-pass dichroic mirror (Chroma Technology, Brattleboro, Vermont). Fluorescence generated by the two-photon spot is collected by the microscope objective in the epi-illuminated geometry. Our near-IR reflecting dichroic mirror then transmits the shorter fluorescence wavelengths. In addition to the dichroic mirror, the fluorescence also passes additional optical filters prior to reaching the photomultiplier tube (PMT). For this study, the PSF was measured using two high numerical aperture (NA) Zeiss objectives: the water immersion, 63 \times C-Apochromat (NA 1.2 Korr; working distance of 0.24 mm) lens and the oil immersion, 63 \times Plan-Neofluar (NA 1.25; working distance of 0.1 mm) objective. For each objective, the maximum imaging

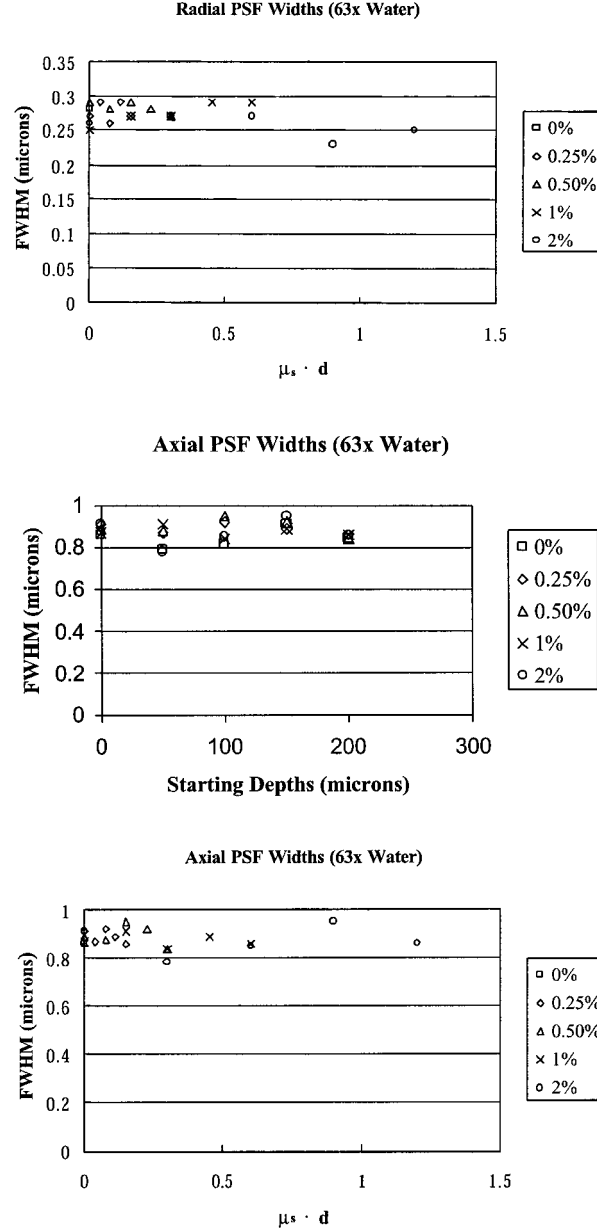


Fig. 5 Averaged widths of the radial and axial PSF from five spheres at four depths and five Liposyn III concentrations (0, 0.25, 0.5, 1, and 2%), taken with 63 \times , water immersion, C-Apochromat objective (NA 1.2). $\mu_s \cdot d$ is the product of the scattering coefficient μ_s and imaging depth d .

Table 1 PSF widths (FWHM) for 63× oil (NA 1.25) and 63× water immersion (NA 1.2) objectives at different starting depths (in microns).

		63× oil			63× water				
		Radial FWHM	SD	Axial FWHM	SD	Radial FWHM	SD	Axial FWHM	SD
Theory ^{2,20}		0.230		0.636		0.240		0.691	
0% 0 μm	$\mu_s \times d = 0$	0.25	0.03	0.73	0.04	0.28	0.03	0.86	0.04
25 μm	0	0.28	0.04	1.30	0.20				
50 μm	0	0.30	0.02	1.40	0.06	0.30	0.04	0.79	0.05
75 μm	0	0.31	0.03	1.88	0.13				
100 μm	0	0.30	0.03	1.86	0.16	0.28	0.02	0.82	0.06
150 μm	0					0.28	0.02	0.91	0.05
200 μm	0					0.28	0.02	0.84	0.07
0.25% 0 μm	0	0.24	0.01	0.75	0.09	0.27	0.01	0.91	0.09
25 μm	0.01875	0.28	0.06	1.26	0.12				
50 μm	0.0375	0.25	0.06	1.23	0.15	0.29	0.04	0.87	0.10
75 μm	0.05625	0.30	0.06	1.76	0.10				
100 μm	0.075	0.33	0.08	2.08	0.28	0.26	0.05	0.92	0.07
150 μm	0.1125					0.29	0.06	0.89	0.06
200 μm	0.15					0.27	0.04	0.86	0.07
0.5% 0 μm	0	0.26	0.01	0.75	0.02	0.29	0.03	0.89	0.09
25 μm	0.0375	0.28	0.05	1.39	0.10				
50 μm	0.075	0.29	0.01	1.37	0.12	0.28	0.03	0.88	0.06
75 μm	0.1125	0.27	0.03	1.90	0.10				
100 μm	0.15	0.28	0.06	1.88	0.40	0.29	0.03	0.95	0.09
150 μm	0.225					0.28	0.02	0.92	0.11
200 μm	0.30					0.27	0.02	0.84	0.07
1% 0 μm	0	0.27	0.03	0.77	0.08	0.25	0.03	0.87	0.06
25 μm	0.075	0.28	0.05	1.39	0.04				
50 μm	0.15	0.31	0.01	1.30	0.05	0.27	0.03	0.91	0.13
75 μm	0.225	0.31	0.04	1.86	0.23				
100 μm	0.30	0.26	0.05	1.73	0.25	0.27	0.02	0.84	0.06
150 μm	0.45					0.29	0.06	0.89	0.07
200 μm	0.60					0.29	0.06	0.86	0.10
2% 0 μm	0	0.24	0.04	0.77	0.06	0.26	0.04	0.91	0.07
25 μm	0.15	0.26	0.02	1.25	0.23				

Table 1 (Continued).

	63× oil				63× water			
	Radial FWHM	SD	Axial FWHM	SD	Radial FWHM	SD	Axial FWHM	SD
50 μm	0.30	0.27	0.06	1.16	0.13	0.27	0.03	0.78
75 μm	0.45	0.30	0.05	1.71	0.28			
100 μm	0.60	0.24	0.06	1.92	0.47	0.27	0.07	0.85
150 μm	0.90					0.23	0.04	0.95
200 μm	1.20					0.25	0.05	0.86
								0.13

Note: The results are obtained from averaging five 0.1-μm microspheres. Theoretical values are also calculated.^{2,28} $\mu_s \times d$ is the product of scattering coefficient μ_s and imaging depth. μ_s is estimated from the comparable Intralipid solution.²⁵

depths were determined by the objectives' working distances. With each objective, we imaged the microspheres to depths nearing the objectives' working distances (100 μm for the oil objective and 200 μm for the water objective).

To achieve three-dimensional scanning at different depths, the objective is first manually moved into the appropriate axial position using the manual dial of the microscope's objective positioner. Then three-dimensional scanning at each sample depth is accomplished by a combination of x-y scanner and a piezoelectric-driven objective positioner in the axial direction (P-721 PIFOC, Physik Instrumente, Germany). The x-y scan of the sample is composed of 256×256 pixels at a resolution of 0.121 μm per pixel step, and the axial scan step is set at either 0.132 or 0.144 μm, depending on the piezoelectric positioner used. Depending on the sample being imaged, 51 or 76 axial scans are acquired to form a 3-D stack. This corresponds to the total axial thickness imaged to be about 6.6 or 10.9 μm, respectively. Note that the axial positions represent the mechanical movement of the stage systems in our microscope. In our data acquisition mode of single-photon counting, photons collected at each pixel are processed by a discriminator unit and recorded by the data acquisition computer. The computer then stores the 3-D image for processing.

The sample prepared consisted of 0.1-μm yellow-green fluorescent microspheres (Molecular Probes Inc., Eugene, Oregon) imbedded in low-melting-point agarose gel (LMP, GIBCO BRL, Grand Island, New York) with different amounts of scatter (Liposyn III @20%, Abbott Laboratories, Abbott Park, Illinois). To prepare the sample, 2% LMP gel is dissolved and mixed with Liposyn III to achieve a final scattering concentration of 0, 0.25, 0.5, 1, and 2%. While in the molten state, a small amount of the 0.1-μm beads are mixed into the gel. The molten sample mixture is then mounted onto a well slide and covered with a glass cover glass (thickness no. 1). After the gel sets, it becomes a static 3-D structure containing fluorescent microspheres and different amounts of scatter. The 63× C-Apochromat water immersion objective is equipped with a correction collar for the cover glass thickness. To obtain the correct collar setting, a uniform fluorescence sample is used to observe the focal spot right below the cover glass. We found that Zeiss's correction collar marks

correspond well with the cover glass thickness used. For the PSF measurements, we adjusted the microsphere concentration so that sufficient microspheres were present within the scanning field. However, the microsphere concentration is sufficiently dilute that most of the spheres are well separated and overlapping of the spheres' PSFs occurs only minimally. In fact, visual examination of the specimen reveals that most spheres are separated by at least 2 to 3 μm.

4 Results and Discussion

A representative three-dimensional scan of the 0.1-μm microsphere sample (0% Liposyn III) taken with the 63× Plan-Neofluar, oil immersion objective is shown in Fig. 2. The data were visually examined and the approximate centroids of five microspheres were identified. To further process the data, the approximate centroids were used as marker coordinates from which the axial PSF data were extracted from the image stack by identifying the maximum pixel intensity of the microspheres at each axial position. The extracted axial distribution is then fitted to a Gaussian model $I(z)$:

$$I(z) = I_{oz} \exp[-(z - z_o)^2 / \sigma_z^2] + C, \quad (1)$$

where I_{oz} is the peak fluorescence intensity, z_o is the axial centroid, σ_z is the axial intensity distribution width, and C is the background. The fitted centroid z_o can then be used to identify the focal plane and the lateral PSF data extracted and fitted to a Gaussian model. The PSF data and the corresponding fit for one representative microsphere are shown in Fig. 3. The two-photon theoretical intensity distribution given by

$$I_{2\gamma}(u, v) = \left| 2 \int_0^1 J_o(v\rho) \exp(-iu\rho^2/2) \rho d\rho \right|^4 \quad (2)$$

is also plotted in the same figure for comparison $u = k(\text{NA})^2 z$ and $v = k(\text{NA})r$ are the respective normalized axial and radial coordinates for wave number k .^{2,28} Qualitatively, Fig. 3 shows that our experimental results agree well with the theoretical prediction.

For a detailed characterization of the PSF widths (FWHM), image data from five beads are processed and the widths of the radial and axial PSFs are averaged. The average

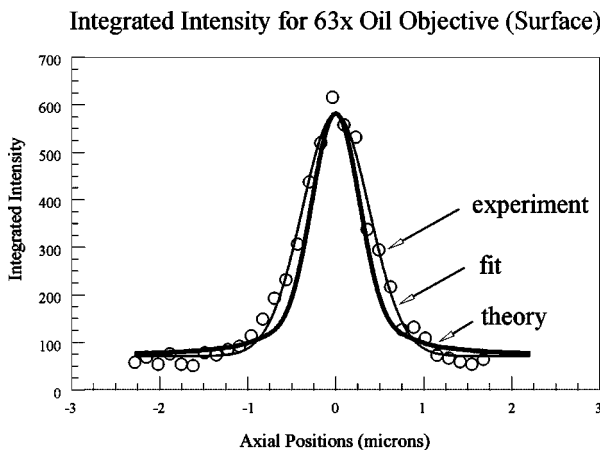


Fig. 6 Representative radially integrated intensity distribution for $63 \times$ oil immersion objective of a $0.1 \mu\text{m}$ fluorescent microsphere.

radial and axial widths (FWHM) of the PSF for the oil objective are plotted in Fig. 4 and the results for the water objective are shown in Fig. 5. A numerical representation of these FWHMs is shown in Table 1. For ease of viewing, the standard deviations of the fitted widths are only shown in the table.

Figure 4, Fig. 5, and Table 1 show that the experimental PSF widths are very different for the oil and water objectives. In the case of the oil objective, our lateral PSF widths vary from 0.24 to $0.31 \mu\text{m}$. These values are slightly larger than the theoretical value of $0.230 \mu\text{m}$. As Fig. 4 shows, there is a tendency for the lateral width to increase with imaging depth. However, there is no indication that increasing scatterer concentration correlates with an increase in lateral widths. For example, at a depth of $100 \mu\text{m}$, the lateral PSF width at the surface is $0.30 \mu\text{m}$ for the 0% Liposyn III sample. At the same depth, the lateral width fluctuates as the Liposyn III concentration is increased from 0.25 to 2% . In the case of the 2% sample, the lateral width is $0.24 \mu\text{m}$, a value 20% less than the surface value. The same fluctuating trend is observed with datasets at other depths, but the fact remains that up to 2% Liposyn III, scattering has no measurable effect on lateral PSF widths. The axial FWHM data demonstrate the same independence of the PSF widths from the scatterer concentration present. However, as imaging depths increase, there is a corresponding increase in the axial PSF widths. For example, in the case of the 0% sample, the axial FWHM increased from 0.73 (at surface) to $1.86 \mu\text{m}$ (at $100 \mu\text{m}$). The degradation of the lateral and axial widths has been reported for oil immersion objectives and is most likely due to spherical aberration.^{22,23,29}

In the case of the water immersion objective, the PSF data are slightly larger than the theoretical value. For the 0% Liposyn III sample, our surface values of the lateral and axial widths are 0.28 and $0.86 \mu\text{m}$, respectively. These values are slightly larger than the corresponding theoretical values of 0.240 (by about 17%) and $0.691 \mu\text{m}$ (by about 24%). An examination of Fig. 4, Fig. 5, and Table 1 shows that the water objective results are very different from those of the oil lens. In the case of the water objective, we also plotted the PSF FWHMs as a function of the scattering parameter μ_s

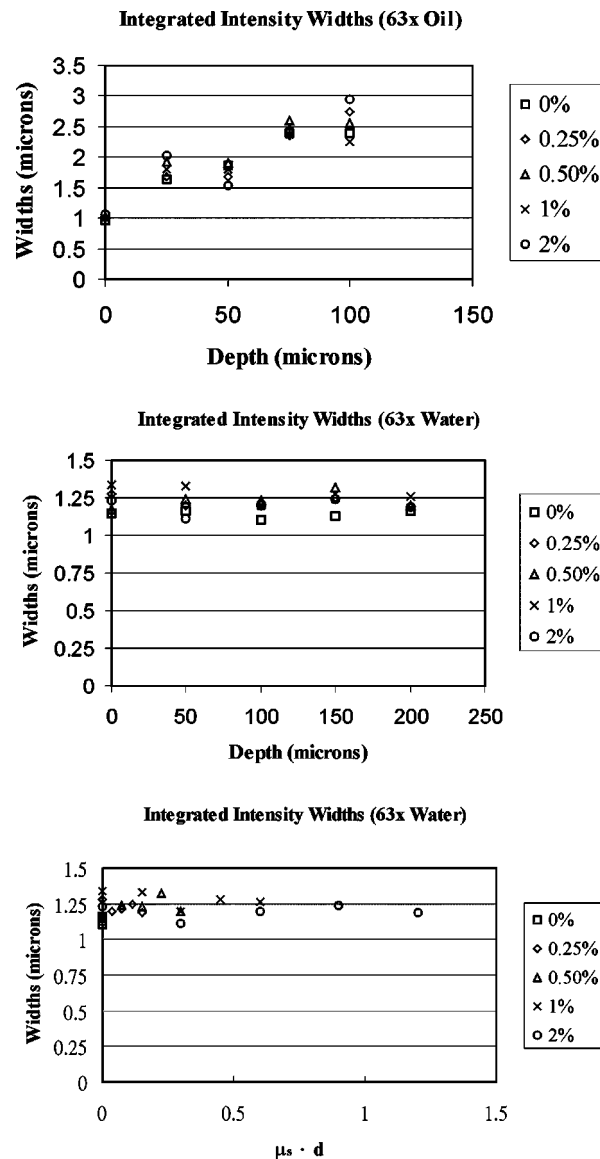


Fig. 7 The FWHMs for radially integrated intensity at different depths for both the $63 \times$ oil and water immersion objectives. $\mu_s \cdot d$ is the product of the scattering coefficient μ_s and imaging depth d .

$\times d$. For the water lens, there is no evidence of the degradation of the PSF width with imaging depths (up to $200 \mu\text{m}$) and Liposyn III concentration (up to 2%). Regardless of the dataset examined, the PSF widths show no obvious correlation with sample depth and scatter concentration. All PSF width values fluctuate around $0.28 \mu\text{m}$ (lateral) and $0.9 \mu\text{m}$ (axial). The spherical aberration-induced degradation of the PSF observed with the oil objective is absent in the water objective data. These results support the fact that the refractive index of the gel closely matches that of water.

In addition to the PSF width analysis, we also calculated the laterally integrated axial intensity profile (LAIP) from the microsphere images. This is accomplished by summing the intensity in a 13×13 pixel region around the approximate centroid of the microsphere. The 169-pixel region corresponds to an area of $1.45 \times 1.45 \mu\text{m}^2$. Since the lateral widths do not appreciably broaden for both objectives (Fig. 4, Fig. 5,

Table 2 FWHMs (in microns) of laterally integrated axial intensity profiles for 63 \times oil (NA 1.25) and 63 \times water immersion (NA 1.2) objectives at different starting depths.

		63 \times oil		63 \times water	
		FWHM	SD	FWHM	SD
Theory		0.676		0.734	
0% 0 μm	$\mu_s \times d = 0$	0.96	0.04	1.15	0.04
25 μm	0	1.63	0.07		
50 μm	0	1.86	0.07	1.16	0.11
75 μm	0	2.40	0.06		
100 μm	0	2.39	0.10	1.10	0.06
150 μm	0			1.13	0.06
200 μm	0			1.16	0.09
0.25% 0 μm	0	1.00	0.06	1.28	0.09
25 μm	0.01875	1.67	0.07		
50 μm	0.0375	1.68	0.08	1.20	0.13
75 μm	0.05625	2.35	0.25		
100 μm	0.075	2.75	0.36	1.21	0.09
150 μm	0.1125			1.25	0.14
200 μm	0.15			1.19	0.13
0.5% 0 μm	0	1.02	0.05	1.17	0.12
25 μm	0.0375	1.92	0.22		
50 μm	0.075	1.90	0.22	1.24	0.10
75 μm	0.1125	2.60	0.24		
100 μm	0.15	2.56	0.56	1.23	0.06
150 μm	0.225			1.32	0.17
200 μm	0.30			1.20	0.12
1% 0 μm	0	1.01	0.08	1.34	0.05
25 μm	0.075	1.80	0.20		
50 μm	0.15	1.81	0.18	1.33	0.21
75 μm	0.225	2.37	0.36		
100 μm	0.30	2.26	0.27	1.20	0.10
150 μm	0.45			1.28	0.13
200 μm	0.60			1.26	0.20
2% 0 μm	0	1.06	0.07	1.23	0.13
25 μm	0.15	2.02	0.20		

Table 2 (Continued).

	63× oil		63× water	
	FWHM	SD	FWHM	SD
50 μm	0.30	1.54	0.12	1.11
75 μm	0.45	2.44	0.89	
100 μm	0.60	2.94	0.68	1.20
150 μm	0.90			1.24
200 μm	1.20			1.19

Note: The results are obtained from averaging five 0.1-μm microspheres.^{2,28} $\mu_s \times d$ is the product of scattering coefficient μ_s and imaging depth. μ_s is estimated from the comparable Intralipid solution.²⁵

and Table 1), the area chosen covers the lateral extent of the PSF and accurately represents the total fluorescence generated at the chosen axial plane. Therefore, the LAIPs can be used to test the extent of image sectioning in our specimen. Our motivation for performing this analysis is the increased sensitivity in detecting PSF degradation. In regions away from the PSF maximum, there may not be sufficient intensity for the PSF to be accurately measured. However, the LAIPs in those regions will have a stronger value and allow a more sensitive analysis of the scattering effect on the PSF. The LAIP for the same 0.1-μm microsphere used for the PSF determination in Fig. 3 is shown in Fig. 6. Comparing Fig. 3 and Fig. 6, one can see that the PSF data reach the background level at about 0.75 μm from the intensity maximum. However, the LAIP did not reach background level until about 1.5 μm from the peak intensity. It is this increase in sensitivity that we hope will allow a more thorough characterization of the PSF in scattering media. For the LAIPs, the Gaussian model is again used to fit the data for their FWHMs. For comparison, the theoretical result given in Refs. 2 and 28:

$$\text{Int}_{2\gamma}(u) = \int_0^{\infty} \left| 2 \int_0^1 J_o(v\rho) \exp(-iu\rho^2/2) \rho d\rho \right|^4 v dv / \int_0^{\infty} \left| 2 \int_0^1 J_o(v\rho) \rho d\rho \right|^4 v dv \quad (3)$$

is also plotted in Fig. 6.

To thoroughly quantify the effect of imaging depths and scattering concentration on the LAIPs, we fitted the distributions for all the microsphere data to the Gaussian model and plotted the LAIP FWHMs in Fig. 7. And in the case of the water immersion objective, we plotted the LAIP FWHMs as a function of the scattering parameter $\mu_s \times d$. The results are also given in Table 2. Our analysis shows the same results as the PSF analysis: up to 2%, the amount of scattering in Liposyn III has no discernable effects on the widths of the LAIPs. For example, in the case of the 63× water objective, the LAIP FWHM at a depth of 200 μm is 1.16 μm (0% Liposyn III sample). At the same imaging depth, results from other scattering samples (1.19 μm for 0.25%, 1.20 μm for 0.5%, 1.26 μm for 1%, and 1.19 μm for 2% Liposyn III) show no sign of PSF degradation caused by increased scattering. Data acquired at other depths also show no correlation of scattering

on the LAIP FWHMs. On the other hand, the LAIP results from the oil immersion objective show the effects of degradation induced by spherical aberration. In this case, the LAIP FWHMs increased from approximately 1 μm at the surface to about 2.5 μm at a depth of 100 μm. Therefore, the additional sensitivity of the LAIPs reveals no scattering-induced degradation of the PSF.

In fact, when we fitted the data for radial widths, axial widths, and laterally integrated intensity widths at each axial position as a function of Liposyn III concentration to a linear model, we found that the slope of the line stayed very close to 0. The magnitude of the slope for most fits is less than 0.1, indicating no correlation between that scattering and the radial PSF, axial PSF, and LAIP widths. Our results demonstrated conclusively that for two-photon imaging down to a depth of 200 μm, scattering due to Liposyn III samples (up to 2%) produces no measurable effects on the two-photon PSF.

5 Conclusion

In this study, we thoroughly characterized the two-photon PSF in turbid medium using oil and water immersion objectives. Tissuelike scattering samples containing Liposyn III (0, 0.25, 0.5, 1, and 2%) and 0.1-μm fluorescent microspheres imbedded in agarose gel were imaged, and the results were analyzed for the radial PSF, axial PSF, and LAIP widths. Our analysis showed that at imaging depths up to 100 μm (oil objective) and 200 μm (water objective), neither the radial nor the axial PSF showed any scattering-induced degradation. The axial sectioning capabilities determined from the LAIPs also appear not to be affected by the scattering concentrations used. The only degradation in the PSF was observed for the oil immersion objective at increased depths, an effect that is most likely due to spherical aberration. Our results support the generally accepted view that the presence of scatterers in tissuelike phantoms does not affect the PSF, and the spatial resolution of two-photon imaging in a turbid medium remains close to the diffraction limits.^{16,25}

References

- W. Denk, J. H. Strickler, and W. W. Webb, "Two-photon laser scanning fluorescence microscopy," *Science (Washington, DC, U.S.)* **248**, 73–76 (1990).

2. C. J. R. Sheppard and M. Gu, "Image formation in two-photon fluorescence microscopy," *Optik (Jena)* **86**(3), 104–106 (1990).
3. *Handbook of Biological Confocal Microscopy*, J. B. Pawley, Ed., Plenum, New York (1995).
4. J. D. Jackson, *Classical Electrodynamics*, Wiley, New York (1975).
5. I. Itzkan and J. A. Izatt, *Medical Use of Laser Encyclopedia of Applied Physics* **10**, 33–59 (1994).
6. B. R. Masters, P. T. C. So, and E. Gratton, "Multiphoton excitation fluorescence microscopy and spectroscopy of *in vivo* human skin," *Biophys. J.* **72**, 2405–2412 (1997).
7. P. T. C. So, H. Kim, and I. E. Kochevar, "Two-photon deep tissue *ex vivo* imaging of mouse dermal and subcutaneous structures," *Opt. Express* **3**(9), 339–350 (1998).
8. D. W. Piston, B. R. Masters, and W. W. Webb, "Three-dimensionally resolved NAD(P)H cellular metabolic redox imaging of the *in situ* cornea with two-photon excitation laser scanning microscopy," *J. Microsc.* **178**, 20–27 (1995).
9. C. Buehler, K. H. Kim, C. Y. Dong, B. R. Masters, and P. T. C. So, "Innovations in two-photon deep tissue microscopy," *IEEE Eng. Med. Biol. Mag.* **18**, 23–30 (1999).
10. W. Denk, K. R. Delaney, A. Gelperin, D. Kleinfeld, B. W. Strobridge, D. W. Tank, and R. Yuste, "Anatomical and functional imaging of neurons using 2-photon laser scanning microscopy," *J. Neurosci. Methods* **54**, 151–62 (1994).
11. W. Denk, M. Sugimori, and R. Llinas, "Two types of calcium response limited to single spines in cerebellar Purkinje cells," *Proc. Natl. Acad. Sci. U.S.A.* **92**, 8279–8282 (1995).
12. K. Svoboda, W. Denk, D. Kleinfeld, and D. W. Tank, "*In vivo* dendritic calcium dynamics in neocortical pyramidal neurons," *Nature (London)* **385**, 161–165 (1997).
13. R. Yuste and W. Denk, "Dendritic spines as basic functional units of neuronal integration," *Nature (London)* **375**, 682–684 (1995).
14. K. T. Jones, C. Soeller, and M. B. Cannell, "The passage of Ca^{2+} and fluorescent markers between the sperm and egg after fusion in the mouse," *Development* **125**, 4627–4635 (1998).
15. J. M. Squirrell, D. L. Wokosin, J. G. White, and B. D. Bavister, "Long-term two-photon fluorescence imaging of mammalian embryos without compromising viability," *Nat. Biotechnol.* **17**, 763–767 (1999).
16. V. E. Centonze and J. G. White, "Multiphoton excitation provides optical sections from deeper with scattering specimens than confocal imaging," *Biophys. J.* **75**, 2015–2024 (1998).
17. S. T. Flock, B. C. Wilson, and M. S. Patterson, "Total attenuation coefficients and scattering phase functions of tissues and phantom materials at 633 nm," *Med. Phys.* **14**(5), 835–841 (1987).
18. W.-F. Cheong, S. A. Prahl, and A. J. Welch, "A review of the optical properties of biological tissues," *IEEE J. Quantum Electron.* **26**(12), 2166–2185 (1990).
19. B. C. Wilson and S. L. Jacques, "Optical reflectance and transmittance of tissues: principles and applications," *IEEE J. Quantum Electron.* **26**(12), 2186–2199 (1990).
20. V. Daria, C. M. Blanca, O. Nakamura, S. Kawata, and C. Saloma, "Image contrast enhancement for two-photon fluorescence microscopy in a turbid medium," *Appl. Opt.* **37**(34), 7960–7967 (1998).
21. C. M. Blanca and C. Saloma, "Monte Carlo analysis of two-photon fluorescence imaging through a scattering medium," *Appl. Opt.* **37**(34), 8092–8102 (1998).
22. C. J. de Grauw, J. M. Vroom, H. T. M. van der Voort, and H. C. Gerritsen, "Imaging properties of two-photon excitation microscopy and effects of refractive-index mismatch in thick specimens," *Appl. Opt.* **38**(28), 5995–6003 (1999).
23. H. C. Gerritsen and C. J. de Grauw, "Imaging of optically thick specimen using two-photon excitation microscopy," *Microsc. Res. Tech.* **47**, 206–209 (1999).
24. J. Ying, F. Liu, and R. R. Alfano, "Spatial distribution of two-photon-excited fluorescence in scattering media," *Appl. Opt.* **38**(1), 224–229 (1999).
25. A. K. Dunn, V. P. Wallace, M. Coleno, M. W. Berns, and B. J. Tromberg, "Influence of optical properties on two-photon fluorescence imaging in turbid samples," *Appl. Opt.* **39**(7), 1194–1201 (2000).
26. S. P. Schilders and M. Gu, "Limiting factors on image quality in imaging through turbid media under single-photon and two-photon excitation," *Microsc. Microanal.* **6**, 156–160 (2000).
27. J. B. Fishkin, P. T. C. So, A. E. Cerussi, S. Fantini, M. A. Franceschini, and E. Gratton, "Frequency-domain method for measuring spectral properties in multiple-scattering media: methemoglobin absorption spectrum in a tissue-like phantom," *Appl. Opt.* **34**(7), 1143–1155 (1995).
28. C. Y. Dong, P. T. C. So, C. Buehler, and E. Gratton, "Spatial resolution in scanning pump-probe fluorescence microscopy," *Optik (Jena)* **106**(1), 7–14 (1997).
29. H. Jacobsen, P. E. Hänninen, and S. W. Hell, "Refractive-index-induced aberrations in two-photon confocal fluorescence microscopy," *J. Microsc.* **176**(3), 226–230 (1994).